AGU ADVANCING EARTH AND SPACE SCIENCES

JGR Solid Earth

RESEARCH ARTICLE

10.1029/2025JB032839

New 2010 Maule Aftershock Catalog Reveals Structure of the Deep Subduction Interface

C. Chalumeau[1,2] and A. Rietbrock[2]

[1]University Grenoble Alpes, University Savoie Mont Blanc, CNRS, IRD, University Gustave Eiffel, ISTerre, Grenoble, France, [2]Karlsruhe Institute of Technology, Geophysical Institute, Karlsruhe, Germany

Key Points:

- We create a new aftershock catalog of 146950 events for the Mw 8.8 2010 Maule earthquake
- We image the fine-scale structure of the band of plate interface seismicity located at 40–55 km depth
- At depth, events form 100 m to km scale streaks aligned along dip, which we interpret as fractures within blocks in a mélange structure

Supporting Information:

Supporting Information may be found in the online version of this article.

Correspondence to:

C. Chalumeau,
caroline.chalumeau@univ-grenoble-alpes.fr

Citation:

Chalumeau, C., & Rietbrock, A. (2026). New 2010 Maule aftershock catalog reveals structure of the deep subduction interface. *Journal of Geophysical Research: Solid Earth*, *131*, e2025JB032839. https://doi.org/10.1029/2025JB032839

Received 1 SEP 2025
Accepted 29 JUN 2026

Author Contributions:

Conceptualization: C. Chalumeau, A. Rietbrock
Formal analysis: C. Chalumeau
Investigation: C. Chalumeau
Methodology: C. Chalumeau
Supervision: A. Rietbrock
Validation: A. Rietbrock
Writing – original draft: C. Chalumeau
Writing – review & editing: A. Rietbrock

Abstract On 27 February 2010, a Mw 8.8 earthquake occurred near Maule in south-central Chile. The subsequent rapid deployment of a dense network of seismic stations on land was able to capture the first year of its aftershock sequence. Here, we revisit this data set using picking Artificial Intelligence tools, a 3D velocity model of the region and double-difference techniques, to obtain a catalog of 146950 well-constrained events. We observe many features first documented by studies using less dense aftershock catalogs, including the presence of important outer rise seismicity in the north, the occurrence of small earthquake sequences in the volcanic arc, the pervasive faulting associated with the Mw 6.9 11 March 2010 Pichilemu earthquake, and the separation of plate interface seismicity into two groups located at 15–40 km depth and 40–55 km depth. We focus on the deeper part of the plate interface seismicity (40–55 km depth), located at the bottom of the seismogenic zone, to investigate its structure. In this region, earthquakes seem to occur primarily on non-overlapping planes existing within a ∼1.6 km thick zone. Many of these events form 100 m to km scale long streaks aligned along dip, which might be linked to the presence of afterslip in the region. We speculate that these small lineations may occur within individual blocks smeared along the subduction interface, or alternatively that they may occur within aligned chains of blocks.

Plain Language Summary Aftershocks of the 27 February 2010, Mw 8.8 Maule earthquake, which occurred in south-central Chile, were captured by a dense network of seismic stations. Here, we reprocess this data set using new techniques capable of producing large, dense and precisely located catalogs of earthquakes. We find that the earthquakes located along the plate interface are separated into two groups based on depth. The deeper group, which we are able to image most precisely, occurs at the downdip edge of the seismically active interface. Earthquakes there form small streaks aligned in the direction of slip, which signal the presence of aseismic slip. We suggest that these streaks occur within blocks smeared or aligned along the plate interface.

1. Introduction

The 27 February 2010 Mw 8.8 Maule, Chile, earthquake ruptured a 500 km long segment of the central Chile subduction zone between ∼34° and ∼38.5°S (Klein et al., 2016; Lorito et al., 2011; Moreno et al., 2012; Yue et al., 2014), with two main large coseismic slip regions to the north and south of the mainshock epicenter (Moreno et al., 2012; Lin et al., 2013) (Figure 1). The rupture likely propagated to the trench in the north around 34°–35°S (Maksymowicz et al., 2017; Yue et al., 2014) and in the south around 37°S (Vigny et al., 2011; Yue et al., 2014). One notable feature of the rupture is the separation between the high-frequency radiation, which occurs at the downdip end of the earthquake rupture (40–50 km depth) (Kiser & Ishii, 2011), and the low-frequency radiation, which is shallower (D. Wang & Mori, 2011). This separation has been linked to a localized decrease in P-wave velocity determined from local earthquake tomography (Hicks et al., 2014), and may reflect a potential change in the structure or composition of the interface (Hicks et al., 2014; K. Wang et al., 2020). Along-strike, the peak in high-frequency radiation seems to correspond to a high-coupling region, while the peak in low-frequency radiation occurs where coupling is lower but coseismic slip is higher.

In the aftermath of the mainshock, aseismic afterslip was recorded primarily downdip of the mainshock (Bedford et al., 2013; Klein et al., 2016; Lin et al., 2013), in regions where the *Vp*/*Vs* ratio at the plate interface and in the slab was high, probably due to the presence of fluids (Hicks et al., 2014; Moreno et al., 2014). Afterslip was found to experience pulses in the months after the mainshock, which may be linked to changes in pore fluid pressure (Bedford et al., 2013).

Journal of Geophysical Research: Solid Earth 10.1029/2025JB032839

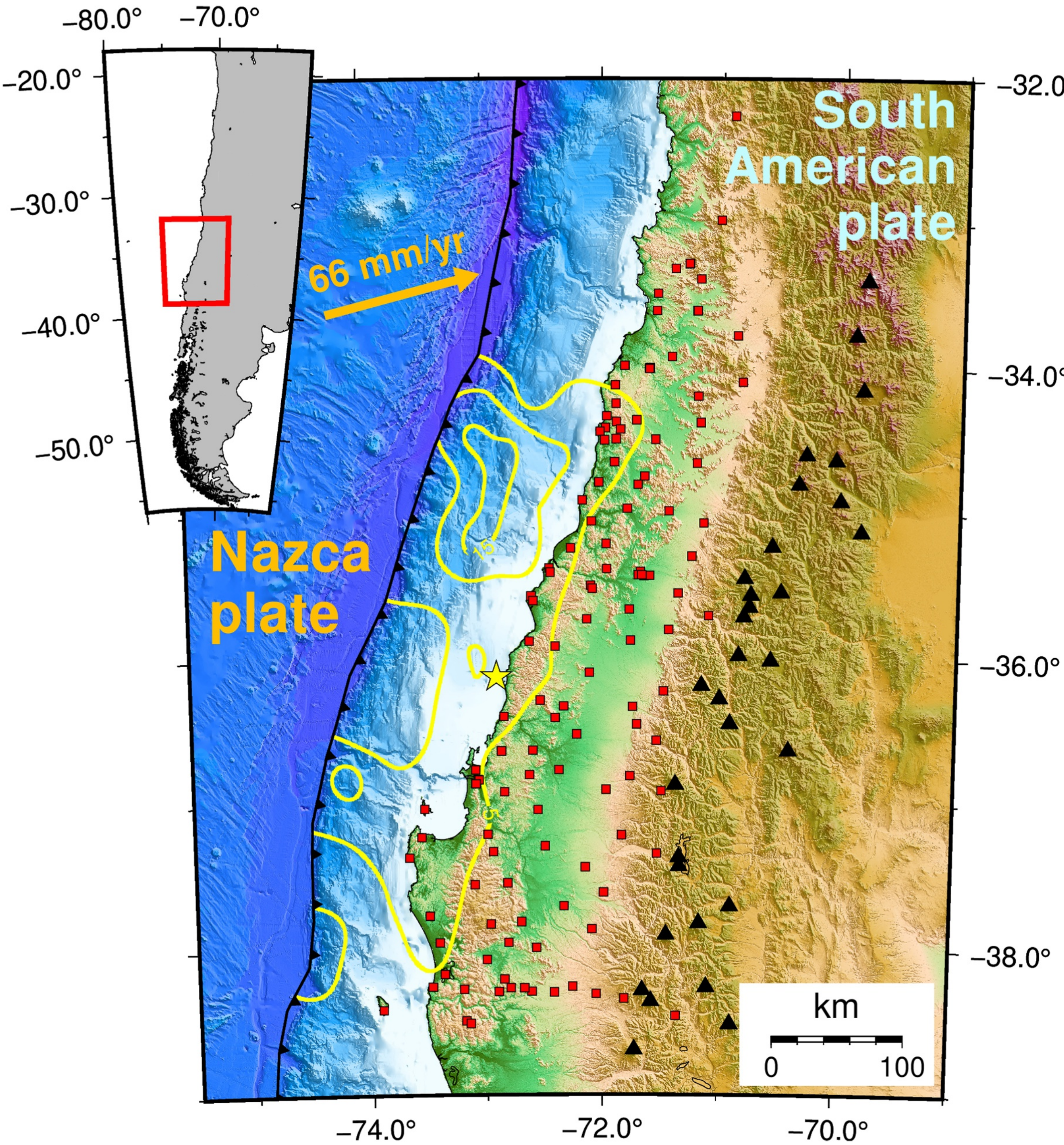

Figure 1. Tectonic context of the 2010 Mw 8.8 Maule earthquake. The yellow star and lines represent the epicenter and 5 m contours of the mainshock (Yue et al., 2014). Red squares are the stations used in this analysis (International Maule Aftershock Data set). Volcanoes are shown as black triangles.

Several authors have compiled catalogs of aftershocks for the Maule earthquake, using the International Maule Aftershock Data set (IMAD) (Hayes et al., 2013; Lange et al., 2012; Rietbrock et al., 2012). These catalogs were created using a mix of manual picking and STA/LTA algorithms (Hayes et al., 2013; Lange et al., 2012; Rietbrock et al., 2012), with the additional use of the MPX picking algorithm in the case of Lange et al. (2012). They showed aftershock activity occurring in the upper plate, in the outer rise region, and at the plate interface. The plate interface events were separated in depth into two regions: the main aftershock region, at 20–40 km depth, and a second region around 40–50 km depth below the downdip edge of the coseismic rupture (Lange et al., 2012; Rietbrock et al., 2012).

We aim to revisit this data set using modern AI techniques to create a denser catalog of seismicity, enabling us to investigate the fine scale structure of a subduction zone interface region. While Chalumeau et al. (2024) used similar techniques to image the fine scale structure of a subduction zone interface seismicity at an unprecedented resolution in the seismogenic zone, we will focus here on the deepest, best-resolved part of the seismicity and investigate the structure of the transition zone, between the seismogenic and the fully creeping portion of the subduction interface.

2. Data and Methods

2.1. Data and Event Detection

For this study, we have used the entirely publicly available IMAD (Roecker & Russo, 2010; Vilotte & RESIF, 2011). This consists of a dense temporary network of 160 mostly broadband land stations deployed about a month after the mainshock and covering the entire onshore extent of the co-seismic rupture. Of these, at least 40 stations remain active at all times between April and December 2010. The station coverage is highest between April and mid June, during which time about 120 stations are active with a station spacing of about 30 km, allowing for a low detection threshold and high location accuracy, especially for landward aftershocks.

We detect events using the machine-learning picker Phasenet (Zhu & Beroza, 2019) trained on the INSTANCE data set (Michelini et al., 2021), which shows good performance in most settings (Münchmeyer et al., 2022). We implement Phasenet through the SeisBench python toolbox (Woollam et al., 2022), and run it on the continuous data from 27 February to 31 December with a probability threshold of 0.2. Phase associations are then performed with HEX, which performs well in situations with many outliers and short interevent times (Woollam et al., 2020). HEX works by randomly fitting hyperbolae to the list of picks within a given time window until it finds a hyperbola that fits a sufficient number of picks. At this stage, we impose a minimum of 6 picks to detect a large number of events. As the vp/vs ratio needs to be fixed, we set it to 1.78, which is within the expected range of values for the region (Hicks et al., 2014). With these parameters, we are able to detect 289625 events, although this likely includes fake detections and unlocatable events, which we will remove in the following steps.

2.2. 1D Location and Quality Check

We use NonLinLoc (Lomax et al., 2000, 2014) and the local 1D velocity model derived by Hicks et al. (2012) for the Maule sequence to get initial locations for events, and to check for event and pick quality. After the initial location, individual picks are removed from an event if their residual is over either 10 s or if it is over 0.5 $+0.0325d$ s, where d is the epicentral distance in kilometers. This cutoff corresponds roughly to the 98th percentile of residuals as a function of distance, allowing us to remove picks that were likely misassociated. Events which still have 12 or more picks are then located again with NonLinLoc.

Along with misassociated picks, we also have instances where a single event is split by the associator into different subevents, especially if the event is detected by both close and distant stations. To remedy this, we merge pairs of events which have an interevent distance below 20 km or the sum of location errors (if it is smaller), a maximum time difference of 6 s, and a maximum of 10% of stations in common for both phases. This is because in cases where we genuinely have two separate but spatially and temporally close events, we would expect them to be detected by the same stations. On the other hand, since the associator can only assign a pick to a single event, earthquakes whose picks have been split into two separate subevents will see little to no overlap in the list of stations for each phase. By combining these three criteria, we can therefore clearly pick out split events. For this step of the procedure, in order to avoid merging fake detections, we only consider events for merging if they have a location error under 30 km, a picking residual RMS below 1 s and at least 17 picks each. Merged events are then located again with NonLinLoc with their new set of picks.

2.3. 3D Relocation

We used Simul2000 (Eberhart-Phillips, 1986; Thurber & Eberhart-Phillips, 1999; Thurber et al., 2009) and the local 3D velocity model derived by Hicks et al. (2014) for this sequence to obtain 3D relocations of events. All station elevations fall between 0 and 1.7 km, and are thus included within the second uppermost layer of the velocity model (-2 to 0 km). Simul2000 does not provide location uncertainties, and is sensitive to initial locations. We therefore test the stability of the final solutions to the initial location by relocating each event using 27 starting locations from -15, $+0$, and $+15$ km from the origin longitude, latitude and depth of the 1D location. Out of the 27 final locations, we select one third of the locations with the largest number of picks retaining a final

10.1029/2025JB032839

Table 1
Parameters Used for Relative Relocation in the Two Runs of GrowClust

	Rmin	Rmincut	RPSavgmin	RMSmax	Ngoodmin	Distmax	Distmax2	Hshiftmax	Vshiftmax
Run 1	0,7	0,7	0,7	1	6	30	5	50	50
Run 2	0,7	0,7	0,8	1	12	30	1	50	50

weight of 0.1 or more in the inversion. Among the selected locations, we consider the best location of a given event to be the one with the smallest pick residual RMS, while the location error is taken as the 95th percentile of the distance between the best location and all other locations with less than the median RMS. By using this approach, we are able to relocate 215582 events. However, to ensure that only real, well-constrained events are kept for subsequent analysis, we retain for this analysis all events with at least 12 picks and a location error under 25 km or at least 30 picks, which amounts to 146950 aftershocks.

2.4. Relative Relocation

To reduce the number of events to correlate, we only consider events for relative relocation if their azimutal gap is below 270°, at least 12 picks including at least 4 P picks and at least 4 S picks, an RMS below 0.6 s and a location uncertainty below 15 km. This amounts to 111419 events, which we are reasonably confident can be relocated well.

Correlations and time delays are calculated on the Z components. Each event pair is considered if they are within 15 km of each other. We filter the signal between 2 and 15 Hz and create windows of −1 to +1 s for the P wave and −1.2 to +1.6 s for the S wave. Before calculating the correlations, we add synthetic picks calculated by NonLinLoc in a 3D velocity model for event-station pairs where we have no machine-learning picks. This is done to maximize the amount of exploitable data, especially in cases where picks have been missed by the picker or the associator. To limit both the calculation costs and the risk of correlating noise, we only calculate correlations if the signal/noise ratio is above 1 for both events, where the noise is calculated in a window ending 1 s before the P wave, with the same length as the window of the phase being considered.

With the differential times calculated from correlations and the 3D velocity model from Hicks et al. (2014), we use GrowClust3D to perform the relative relocations (Trugman & Shearer, 2017; Trugman et al., 2023), as it is able to quickly and efficiently process large amounts of data and supports the use of a 3D velocity model. While other relative relocation algorithms like HypoDD (Waldhauser & Ellsworth, 2000) offer the possibility of using several relocation iterations to gradually refine locations by altering weights and thresholds for the data, GrowClust3D does not. For our data set however, we find that there is a tradeoff between the location precision and the number of earthquakes that can be relocated, due to parameters like the correlation threshold (RPSavgmin), the required number of differential times (Ngoodmin) and even the maximum distance two clusters are allowed to be to merge together (Distmax2). Having a high RPSavgmin and Ngoodmin and a low Distmax2 ensures the greatest stability and precision at small scales (10–100 m), but cuts out most of the events and limits the resolution of larger-scale structures (100 m–1 km), since clusters are not connected. Thus in order to relocate the largest number of events while also optimizing the precision of the locations when possible, we run two GrowClust iterations (Table 1). The first iteration is run on all events using the 3D absolute locations as input, while the second iteration is run taking the first iteration results as input in order to improve them. In total, 61750 are relocated in iteration 1, of which 34271 are also relocated in iteration 2. The median total relative location error for iteration 1 is 821 m, while it is 31 m for iteration 2.

2.5. Magnitudes

Absolute local magnitudes are calculated using a time window from −3 s to +12 s after the S arrival for each event. Like for the catalog of Rietbrock et al. (2012), the local magnitude is defined after Bakun and Joyner (1984) as: $\mathrm{Ml} = \log 10(A) + \log 10(\mathrm{dist}/100) + 0.00301*(\mathrm{dist} - 100) + 3$ Where dist is the distance in km and A is the peak-to-peak Wood-Anderson amplitude of the signal in mm. Due to the large number of events occurring at the same time, we sometimes have issues with magnitudes being overestimated. We use several strategies to reduce these biases. First, we only use stations for which the signal-to-noise ratio is above 3, to limit the impact of noise on the amplitude estimations (Figure S1a in Supporting Information S1). In this case, the noise window is also

10.1029/2025JB032839

15 s long, and ends 2 s before the P arrival. This does not however remove all erroneous magnitudes, especially in cases where a second event arrives at the station in the window we use to calculate the magnitude of the first event (Figure S1b in Supporting Information S1). This is why for each event, we also use the moveout of amplitude and signal-to-noise ratio as a function of distance in order to remove outlier stations. For a given event with at least 6 measurements, assuming a constant noise at all stations, we fit the equation $\log10(S/N) = \log10(10^{**}(C - \log10(\text{dist}/100) - 0.00301^{*}(\text{dist} - 100) - 3) + 1)$ to our signal-to-noise ratio moveout and remove stations which are more than twice the standard deviation from the predicted value of S/N. We also do not calculate magnitudes for events where the amplitude or the signal-to-noise ratio increases with distance. Once all these checks have been performed, the magnitude of an event is taken as the median value from all acceptable stations. As a final step, we refine our magnitudes and incorporate more events by calculating relative magnitudes following the method by Schaff and Richards (2014). As a byproduct of the correlations, we record the signal amplitude difference between events for both the P and the S phase. We use these amplitude differences as magnitude differences if the correlation coefficient is above 0.7, and we use a least squares inversion incorporating both absolute magnitudes and pairwise magnitude differences to invert for the final magnitudes of the catalog.

3. Main Features of the Seismicity

3.1. Comparison to Other Catalogs

As mentioned, Rietbrock et al. (2012) and Lange et al. (2012) have both produced catalogs of this sequence using more traditional picking techniques like manual picking and STA/LTA. Lange et al. (2012) uses a shorter time period of April–September 2010 and finds 13441 events with at least 12 P picks, while Rietbrock et al. (2012) examines the April–December 2010 period (like our study) and finds 40087 events. Thus our catalog, which comprises 146950 events, more than triples the number of events found.

Most of the patterns of seismicity are similar across the different catalogs. The temporal evolution of seismicity in all cases is similar, showing an overall decrease over time that is strongly modulated by the number of available stations (Figure 2). Normalizing the number of earthquakes per day by the number of stations available does show that the seismicity overall decays with time (Figure 3).

We see more differences in magnitudes catalogs (Figure 4). Our magnitudes are overall lower than those of Rietbrock et al. (2012) by about 0.5, but the *b*-values are around 1.2 for both populations, while the Lange et al. (2012) magnitudes have a significantly different distribution with no clear *b*-value or magnitude of completeness but are similar for the largest events. Differences in calculated magnitudes between ours and the Rietbrock et al. (2012) catalog might be attributable to a difference in methods, as we remove stations deemed too noisy and use relative magnitudes. While the magnitude of completeness is similar between our catalog and the Rietbrock et al. (2012) catalog once adjusted to account for the absolute magnitude difference, we do still recover significantly more low-magnitude earthquakes. This is explained by the fact that the magnitude of completeness is improved onshore, especially in the north, but not necessarily offshore, especially in the center and south (Figure S2 in Supporting Information S1). As our workflow removes events that are too poorly located, this might reflect the difficulty that we have in relocating offshore events, especially in the south where fewer stations are active and where the azimuthal gap is particularly large in the outer rise, or in the center where the station network changes over the study period (Figure S3 in Supporting Information S1).

Finally, patterns in the locations tend to be similar between the three catalogs, although more events means spatial features can become more visible. We will now focus on the main groups of seismicity (Figure 5).

3.2. Outer Rise Seismicity

We observe outer rise events along the length of the rupture, with the largest concentration in the north (34S-35S), and another large cluster in the south (38S). However, these events tend to have uncertain locations, with depths in particular being very poorly constrained, as we would expect outer rise events to occur within the first 10–20 km (Lieser et al., 2014; Ruiz & Contreras-Reyes, 2015). Although some studies have been able to better constrain earthquake locations in the north thanks to a temporary Ocean Bottom Seismometer deployment (Lieser et al., 2014), we did not use these stations as their data is not public and only covers a few months. Thus the large azimuthal gap combined with the large distance to the coast makes most offshore events difficult to locate, especially in the outer rise and especially in the south (grey cluster at 38S in Figure 5a). In the future, this could

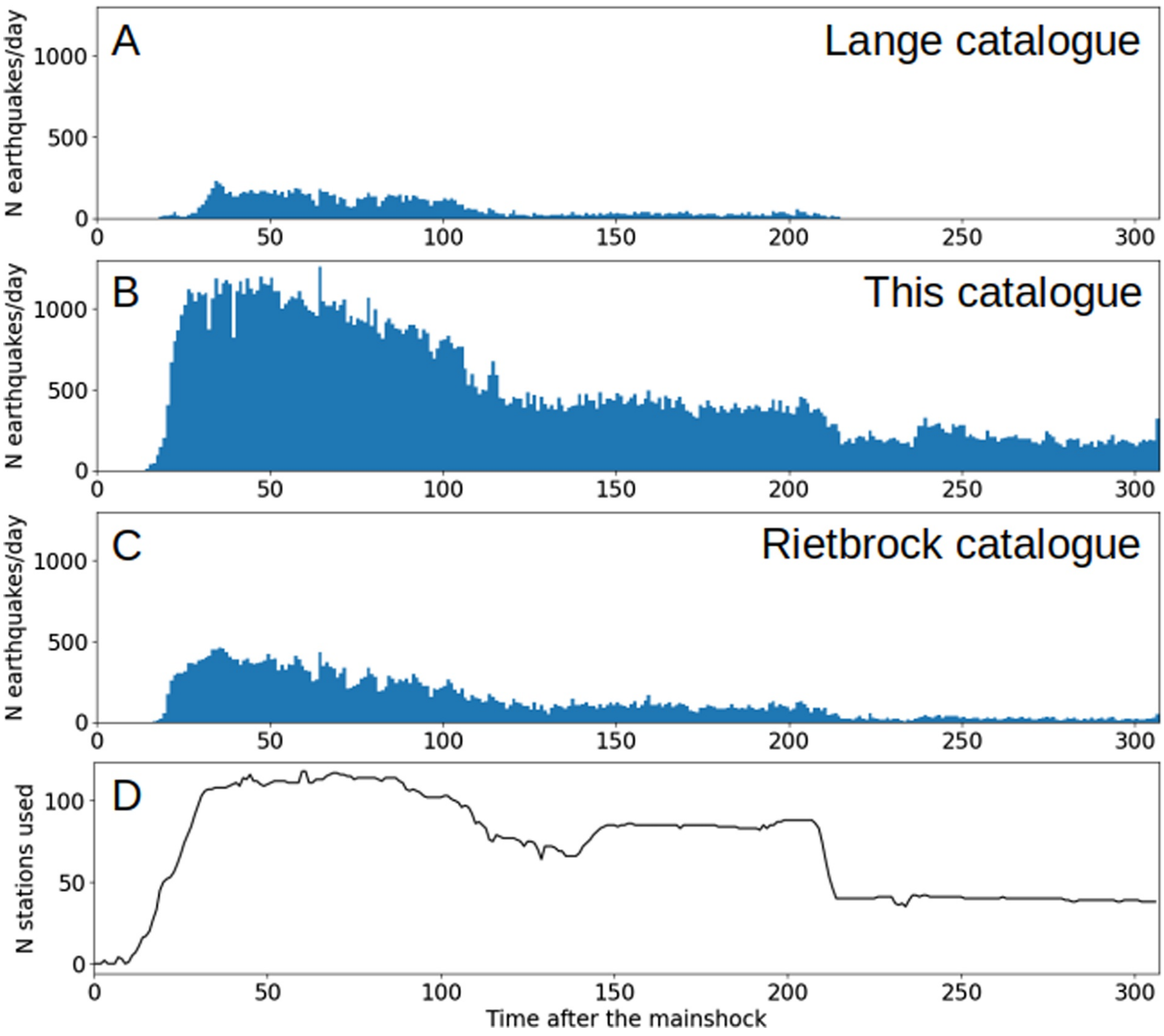

Figure 2. Number of earthquakes per day for: (a) the catalog by Lange et al. (2012), (b) this catalog, and (c) the catalog by Rietbrock et al. (2012). (d) Number of active stations per day.

perhaps be remedied by picking secondary phases and including them in the relocation procedure, as has been done in a few other subduction zones (Aguilar-Suarez & Beroza, 2025; Umino et al., 1995).

Regardless of the unconstrained depths, the presence of outer rise events in itself indicates that the rupture likely reached the trench (Sladen & Trevisan, 2018). Based on the number of earthquakes detected, we can expect the largest amount of slip at the trench in the north at 34S-35S, and a smaller amount in the south at 38S, which is in accordance with models like Yue et al. (2014) or Vigny et al. (2011). Earthquakes in the south (38S) could also be related to the presence of the Mocha fracture zone entering subduction, which could have acted as a plane of weakness in the oceanic plate (Ruiz & Contreras-Reyes, 2015).

3.3. Intermediate Depth Seismicity

1657 events occur near the slab below 60 km depth and are thus classified as intermediate depth. Around 35S-36S, they form a clear band about 250 km from the trench that fades south of 36S (Figures 5a and 5h). These events do not seem to exhibit the temporal decay observed in the rest of the catalog (Figure 3), suggesting that they may be relatively insensitive to stress changes and thus independent from large megathrust earthquakes (Wimpenny et al., 2023). Intermediate earthquakes are often linked to dehydration (Kirby et al., 1996; Nacif al., 2015; Wimpenny et al., 2023), and indeed their depth of 70–110 km here is consistent with the area of water loss derived

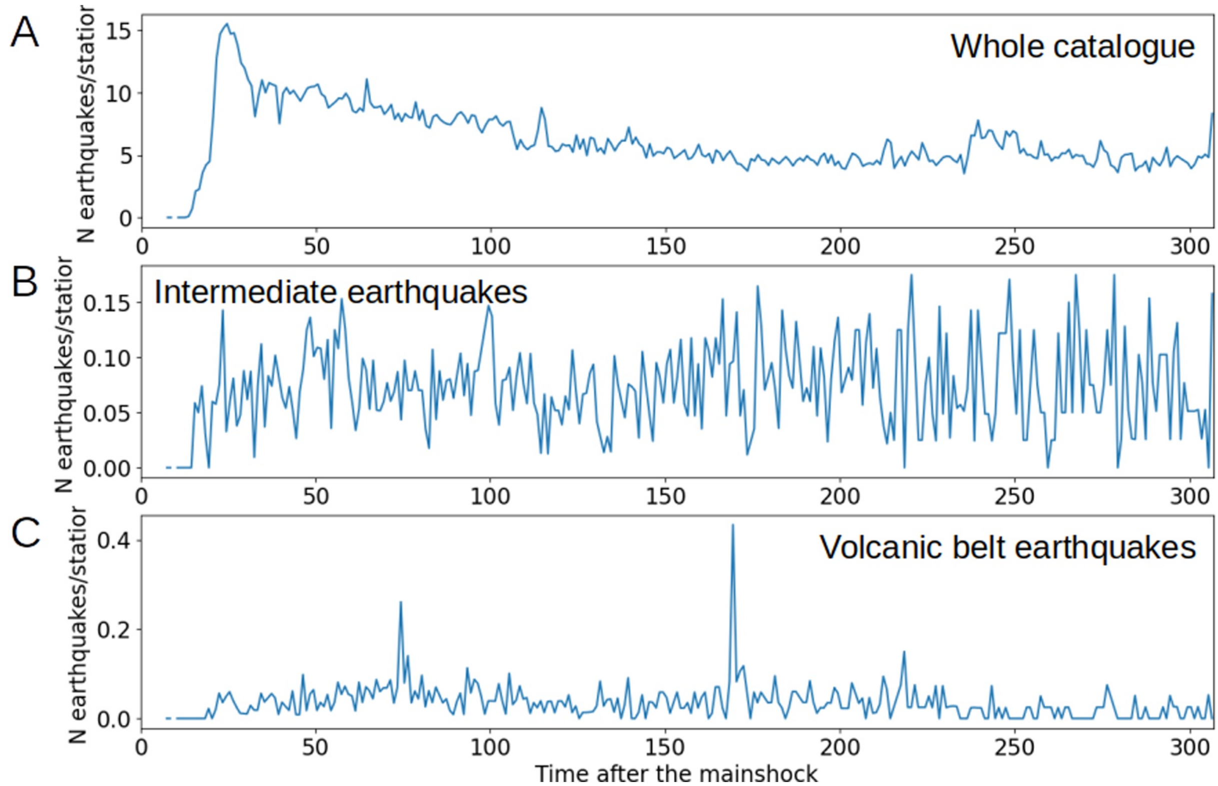

Figure 3. Number of earthquakes per day per available station for (a) Full catalog, (b) only intermediate-depth events, (c) Only events located in the volcanic arc.

by van Keken et al. (2011). However, in our case they occur about 50 km west of the volcanic belt, making the connection less clear.

The decrease of intermediate seismicity from north to south is also notable, as it cannot be explained by differences in the network. In fact, several other studies looking at different time periods with denser station networks find a decrease in intermediate seismicity toward the south starting from 36 S (Bohm et al., 2002; Campos et al., 2002). High magnitude intermediate seismicity in particular decreases toward the south (Campos et al., 2002; Lange et al., 2007), which probably explains our observations. Meanwhile, north of 35S, seismicity no longer increases with latitude (Nacif et al., 2015), probably due to the influence of the flat slab north of 33°S. Several factors can explain this dependence on latitude. First, intermediate seismicity rates in the north may be caused by increased hydration due to more or deeper damage in the downgoing plate, especially in the outer rise (Boneh et al., 2019). Another factor to consider is temperature, as a young lithosphere with high heat flow produces few or no intermediate or deep seismicity (Kirby et al., 1996). As the plate becomes younger toward the south, this probably explains the lower seismicity (Agurto-Detzel et al., 2014).

3.4. The 11 March 2010 Pichilemu Sequence

Among the aftershocks of the Maule earthquake, two normal faulting earthquakes of Mw 7 and Mw 6.9 occurred on 11 March 2010 near the city of Pichilemu within 15 min of each other. The two earthquakes and their afterslip occurred on a pair of faults in synthetic configuration dipping to the SW (Ryder et al., 2012), with the first fault extending from the surface down to about 22 km and the second fault being buried and extending from a depth of 8–20 km. They were likely caused by high Coulomb stress changes from the Maule earthquake (highest in the region) combined with fluids (Farías et al., 2011; Ryder et al., 2012), as the stress field changed from compressional to extensional in the region (Ryder et al., 2012). They triggered their own aftershock sequence just north of Maule's peak slip area, which accounts for about 60634 events, or 40% of the well-constrained catalog (Figures 5f and 5g). This sequence spans from the plate interface to the near surface, with an orientation similar to the strikes of the main doublet. By looking in more detail, we can distinguish 3 distinct zones of seismicity in the area. Some of the seismicity is occurring at the plate interface (Z1), at about 25–30 km depth. Above it is a band of

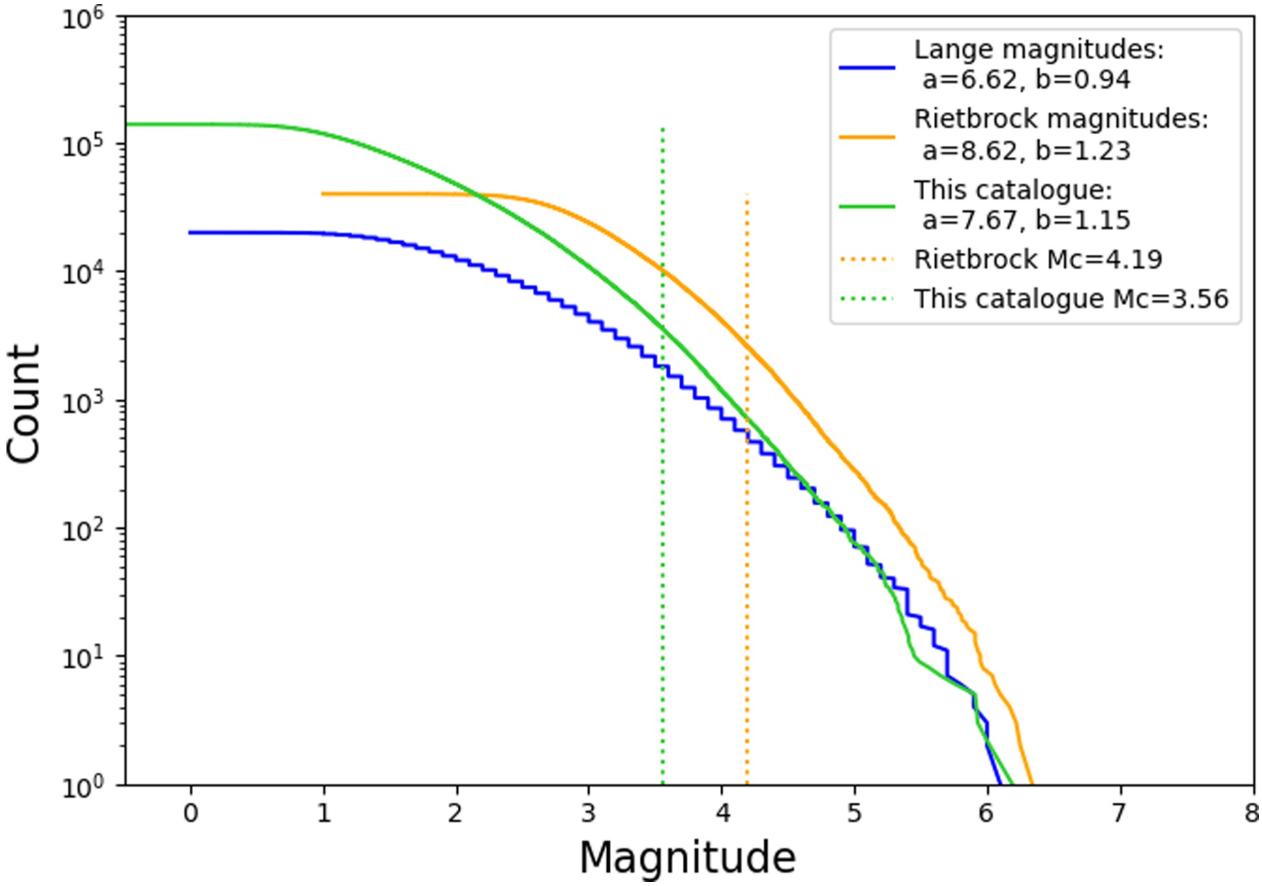

Figure 4. Gutenberg plot for this catalog in green, the catalog from Lange et al. (2012) in blue and the catalog from Rietbrock et al. (2012) in orange. When possible to compute, the magnitudes of completeness are indicated as vertical dotted lines. The magnitudes shown are local magnitudes.

seismicity at 10–25 km depth (Z2), dipping at the same angle as the plate interface but clearly separated from it by a seismic gap. Another band of seismicity is found further up at 0–10 km (Z3), this one flat and perpendicular to the fault strike in the south.

The very high density of seismicity in this area is likely related to pervasive fracturing of the medium. Indeed, Calle-Gardella et al. (2021) found that small-magnitude events have a large variety of focal mechanisms, and a lot of seismicity, including the lower band, occurs in an area with low *Vp*/*Vs* and low *Vp*. However, fluids may also play an important role, as Maule may have increased fluid flow in the forearc (Farías et al., 2011). In particular, the seismic gaps, especially the one between the Z1 and Z2, seem to correspond to areas of low *Vp* but high *Vp*/*Vs* (Calle-Gardella et al., 2021), hinting at the role of fluids, and possibly fluid-triggered aseismic slip, in controlling the spatial distribution of the seismicity.

3.5. Volcanic Arc Seismicity

About 895 events occur at shallow depth in the volcanic arc region, mostly between −37 and −34 S (Figure 5a). Their activity decays very weakly if at all with time, indicating that they are mostly independent from the rest of the aftershock sequence. Instead, two peaks of activity can be found: the first appears to be some swarm-like activity around 36.5 S in the first 4 months, with a peak of activity on the 2010-05-12. The second is a small aftershock sequence caused by a Mw 5.4 earthquake on 2010-08-15T07:50:34 at −36.98.

This is not to say that the Maule earthquake had no impact on volcanic activity and volcanic arc seismicity. Although there is no evidence for multiple volcanic eruptions in the weeks to months after the 2010 earthquake (Pritchard et al., 2013), the Planchón–Peteroa, Nevados de Chillán and Callaqui volcanoes did experience unclamping due to the Mw 8.8 2010 earthquake, which encouraged volcanic activity to a maximum distance of

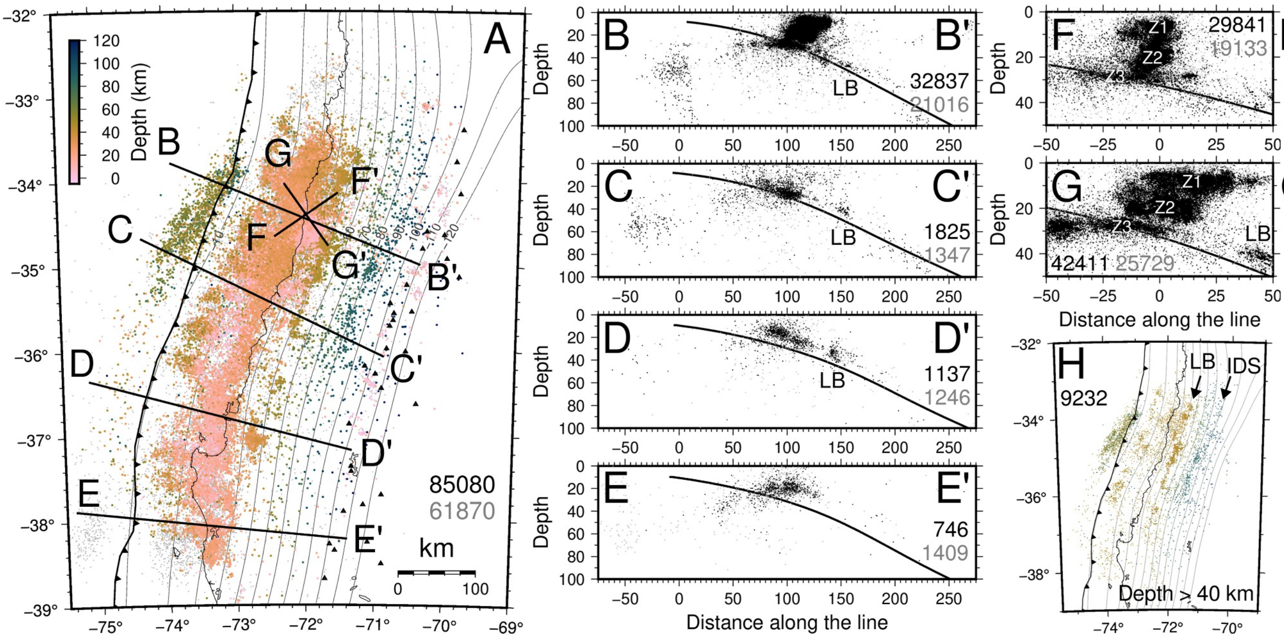

Figure 5. Distribution of the seismicity. (a) shows a map of seismicity. Well-located events with at least 20 picks including 4 P and 4 S and an azimuthal gap of under 270° are colored by depth while less well located events are shown in grey. In the bottom right are shown the number of well-located (black) and less well-located (grey) events. (b–g) are cross-sections with well-located events shown in black and less well-located events shown in grey. Z1, Z2 and Z3 refer to the three main clusters of seismicity that make up the Pichilemu sequence. The section intersects the trench at 0 km. Panel (h) is a map of well-located events below 40 km depth. The lower belt (LB) label refers to the location of the LB of interplate seismicity. The IDS label refers to the location of the intermediate depth seismicity.

251 km (Bonali et al., 2013). Subsidence of up to 15 cm was also observed in five volcanic areas within weeks of the earthquake (Pritchard et al., 2013), perhaps related to coseismic release of fluids from hydrothermal systems. This led in some places to short-term increases in the number of local crustal events, as was observed close to Llaima volcano (Franco-Marín et al., 2023). These are however not related to the volcanic system (Franco-Marín et al., 2023). Similarly, between 35° and 36°S, seismicity clearly increased after Maule due to unclamping on crustal faults (Spagnotto et al., 2015), but again the seismicity is not directly related to the volcanic system. Overall, the area of largest positive coseismic stress change calculated by Spagnotto et al. (2015) on NNW-trending dextral/normal faults corresponds well to the area where we see the highest seismicity rate in our time period, demonstrating the influence of the mainshock on the volcanic arc seismicity.

3.6. Plate Interface Seismicity

The plate interface seismicity occurs in two broad depth clusters. Most events occur where the slab is between 15 and 40 km depth, while a detached, lower belt (LB) of seismicity occurs where the slab is between 40 and 55 km depth and accounts for 11503 events (Figures 5a and 5h). Overall, the plate interface seismicity broadly follows Slab 2.0, but is generally located above it, especially south of 36.5 S. It should be noted however that events far offshore have erroneous depths, and so appear deep in the slab in spite of their thrust mechanisms (Agurto et al., 2012). In spite of location errors, there still is a sharp limit updip as already noted by Lange et al. (2012), where Slab 2 is at 10–15 km depth. This corresponds to a lithological change that is the limit between frontal accretionary prism and backstop (Contreras-Reyes et al., 2008; Hicks et al., 2014; Moscoso et al., 2011), and is likely the top of the seismogenic zone.

In contrast, the LB has much lower location errors, especially for the relative locations, thanks to its position underneath the network. It forms a relatively continuous band containing some high density clusters north of 36 S, while further south we only see a few discontinuous clusters which entirely disappear south of 37 S. It is unclear why this belt of seismicity exists. Previous authors have noted its spatial correlation with afterslip (Klein et al., 2016; Lin et al., 2013) and high frequency radiations from the mainshock (Palo et al., 2014), as well as with the upper edge of the mantle wedge (Dannowski et al., 2013; Hicks et al., 2014). The velocity structure of the area may also provide a clue, as the inter-belt gap appears to coincide with a high-*vp* body in the upper plate while the

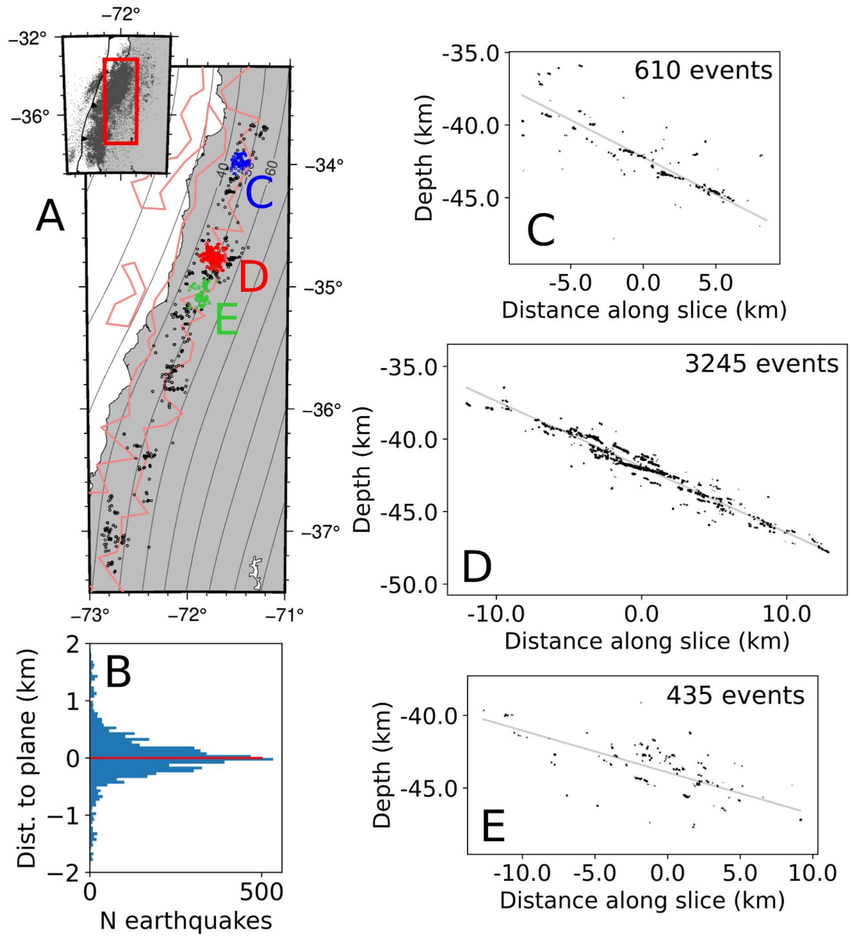

Figure 6. Cross-sections of the lower belt (LB). (a) Map of the LB and the main clusters of seismicity. The pink contours show where the plate interface is distributed according to Cubas et al. (2022), likely reflecting regions of underplating. (b) Histogram showing the distribution of earthquakes with location errors <75 m, relative to the best-fit plane, combining all latitude bins. (c–e) Cross-sections of earthquakes with location errors <75 m.

LB is associated with a localized area of low *vp* on the plate interface and high *vp*/*vs* (Calle-Gardella et al., 2021; Hicks et al., 2014), along with low resistivity (Cordell et al., 2019). This velocity separation also becomes less prominent below 37 S, which may be linked to the disappearance of the LB in the south. As such, some authors have explained the presence of the LB with local fluid overpressure (Cordell et al., 2019; Hicks et al., 2014). Others have posited that the transition from lizardite to antigorite in the mantle wedge could explain this sudden reappearance of seismicity at depth (K. Wang et al., 2020).

4. Structure of the Transition Zone

We aim to better understand the structure of the interface in the deeper belt by examining some of the highest-quality events. In total, 90% of our seismicity tends to occur within a ∼1.6 km thick region (Figure 6b), but in detail seismicity is organized differently in different regions (Figures 6c–6e). In Figure 6c seismicity is relatively diffuse but seems to concentrate primarily in a narrow region. In Figure 6d, where seismicity is the densest, it occurs in a thinner region overall, but seems to be distributed within that region on several planes dipping slightly shallower than the interface. Figure 6e, which is less dense, seemingly shows seismicity occurring on different planes as well. These seemingly subparallel planes of seismicity (Figure 6d) could represent multiple subparallel faults forming a network in a broadly deforming region. They could also represent disconnected neighboring faults with little to no overlap, perhaps separated by more ductile material, or even a single fault with topographic variations causing it to appear as multiple fault planes in cross-section. To determine whether these faults tend to

10.1029/2025JB032839

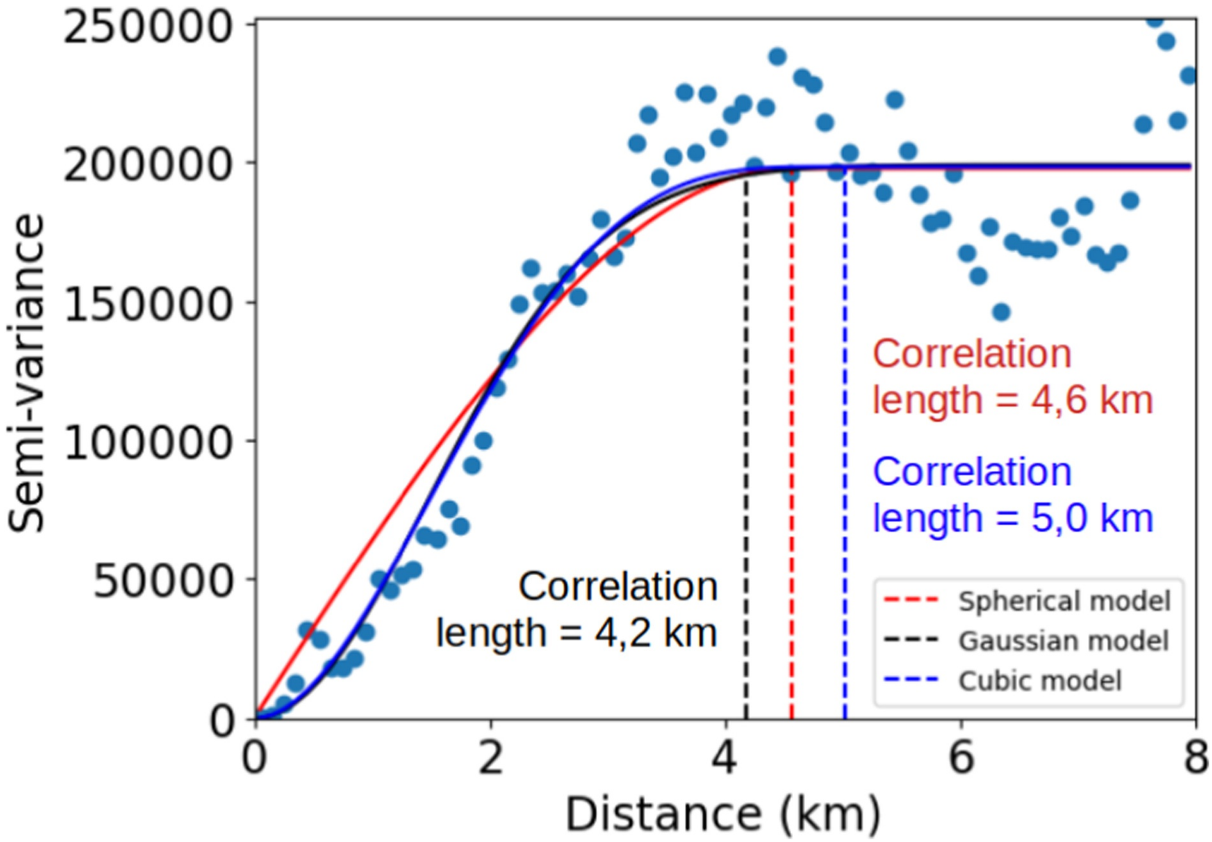

Figure 7. Semivariogram of the difference in elevation between a given pair of events relative to the interevent distance. Three models fit the data reasonably well: a spherical model (red), a gaussian model (black) and a cubic model (blue). Correlation lengths are shown for all three models as dashed lines.

overlap, we calculate the thickness of the seismicity as the interevent distance projected on the slab tends toward 0.

To do so, we first create overlapping bins of our events by latitude, with a bin width of 0.1° latitude and an increment of 0.025° latitude. If there are at least 50 events in a given bin, we fit a plane to all events with a relative location error below 75 m in order to define the plate interface. We then compute for each pair of events with a relative location error under 100 m the elevation difference, which we use to create a half-variogram of the whole LB (Chalumeau et al., 2024). The half-variogram is defined as:

$$\gamma(d) = \frac{1}{2N(d)} \sum_{i=1}^{N} [h(x_0 + d) - h(x_0)]^2$$

With h(x_0) the elevation of a given earthquake relative to the plane, and h($x_0 + d$) the elevation of another earthquake at a distance d. $N(d)$ is the number of pairs at a distance d, and $\gamma(d)$ is the semi-variance of the elevation difference as a function of inter-event distance. Assuming that elevations from the plane are normally distributed, the half-variance of the difference in elevation is equal to the variance of the elevation itself. Thus by modeling the half-variogram, and extrapolating that value to an interevent distance of 0, we can recover the thickness of the seismic layer, which we define as 4 times the standard deviation of the elevation at zero-offset. Here, the half-variogram is computed every 100 m over 8 km, using 2599517 pairs in total (Figure 7).

Our data is best fit by a cubic model which predicts a thickness of less than 1 m, and both the best-fit gaussian and spherical models give a similar estimate. This implies that the faults we observe generally do not overlap in this region, and that the seismic deformation is usually concentrated in a meters-thick region. This can also be seen in zoomed-in cross-sections (Figure 8 and Figure S4 in Supporting Information S1, Data Sets S1–S12 in Supporting Information S2). In some cases, the variations seen in cross-section can be attributed to either location uncertainty

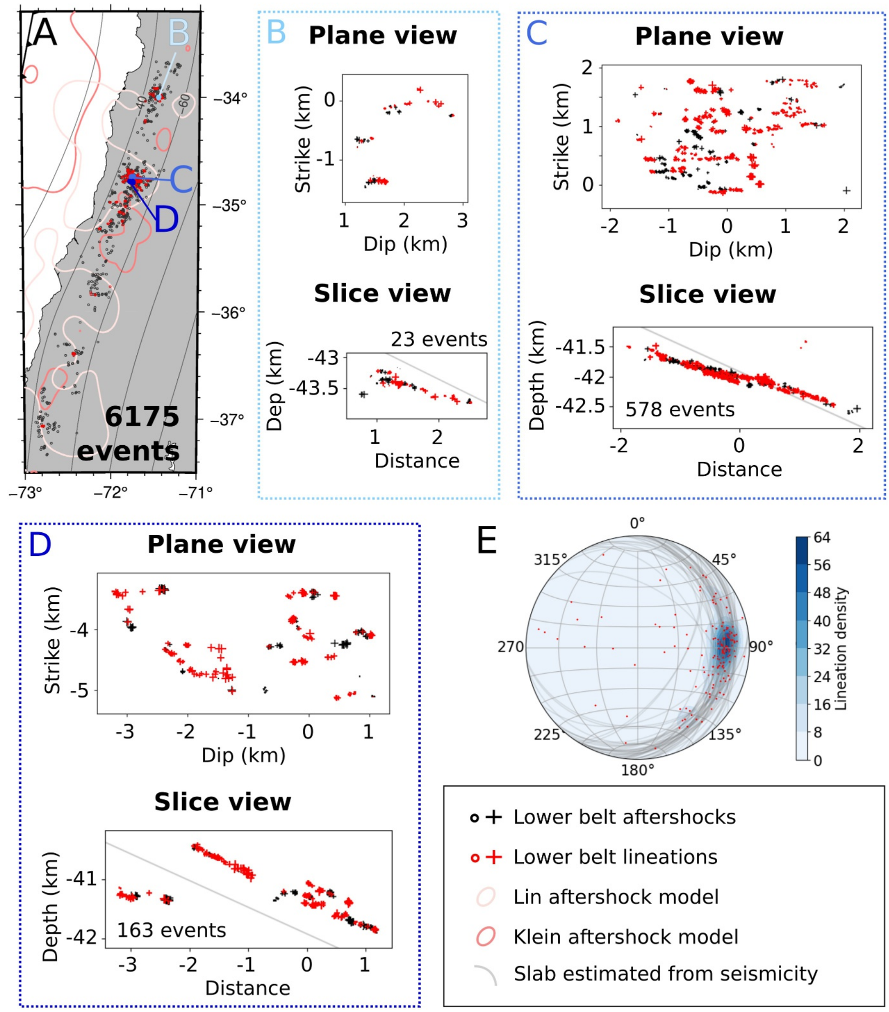

Figure 8. Map and cross-sections of earthquake lineations. (a) Map showing the lower belt (LB) events (black), including the events contained within lineations (red). The 50 cm afterslip contours are shown for two models by Klein et al. (2016) and Lin et al. (2013). (b–d) Small clusters shown projected onto the plate interface (top) and in cross section (bottom). Crosses represent earthquake location errors. (e) Stereonet representing the orientation of earthquake lineations in the LB. Red crosses show lineations, while grey lines show the orientation of all fitted planes within the LB. The blue background represents the density of earthquake lineations.

(Data Set S9 in Supporting Information S2) or topography on a single fault plane (Figure 8c and Figure S4c in Supporting Information S1, Data Set S2 in Supporting Information S2). In others, clusters of seismicity that seem to occur on different planes are laterally separated by a few hundred meters (Figure 8d and Figure S4d in Supporting Information S1, Data Set S3, S4, and S10 in Supporting Information S2), suggesting the existence of distinct, non-overlapping faults. In some rarer cases (Data Set S8 in Supporting Information S2), these fault planes do seem to overlap, confirming the presence of multiple faults.

This observed structure and thickness of the deformation is somewhat different to what was observed in Ecuador by Chalumeau et al. (2024), where seismicity seemingly formed a fault network at the plate interface, with overlapping planes in several places. This might be explained by the different settings, as the Ecuadorian study was done at 20 km depth, within the seismogenic zone though on its lower side. Here by contrast we are in the transition zone between the seismogenic zone and the fully creeping interface, and we expect a large portion of the slip to be aseismic.

The region in and above the LB is thought to host underplating (Figure 6a) (Cubas et al., 2022). Although we might expect this to cause the formation of two active interfaces at the top and bottom of a slice being underplated, we do not see this on a large scale in our region. This could be explained in several ways. It is possible that the underplating region identified by Cubas et al. (2022) is instead confined to the seismic gap updip of the LB, explaining the presence of a high-velocity, high-resistivity body in that region (Cordell et al., 2019; Hicks et al., 2014). Alternatively, it is also possible for a region with documented underplating to have seismicity occurring on a single interface (Kimura et al., 2010). This is likely because underplating is a transient process recurring on large timescales and thus involving periods when the deformation is concentrated on a single interface (Menant et al., 2020). Thus our data implies that no underplating is currently happening in the LB region, but does not exclude that it could happen at different times.

Zooming into the seismicity, we observe that earthquakes form small lineations oriented in the dip direction (Figure 8). To classify earthquakes into these lineations, we first take, for each earthquake, every other neighbor within a 900 m radius. If there are at least 3 neighbors, and the largest distance is at least 300 m, we calculate their plunge and bearing with respect to the central earthquake, and determine whether there is a dominant orientation with fisher statistics. If the probability is above 80%, the angle error below 20° and the kappa above 5, we include in a group all events with an angular distance <20° from the main orientation. Finally, we merge groups if they have events in common and have an angular distance of less than 20°. We thus classify about 20% of events within these lineations.

These types of features are not unique to our setting, as they were first observed by Rubin et al. (1999) in the San Andreas Fault, where streaks were 500 m–2 km long and almost horizontal, and have been seen in other contexts (Rubin et al., 1999). In particular, these features are similar to the streaks of tremor observed in subduction zones (Ghosh et al., 2010; Ide, 2010), suggesting that the environment of the LB may be similar to the environment where Episodic Tremor and Slip occur, although the length scale of these striations are very different (100 m scale for our catalog earthquake streaks, 10 s of km scale for these tremor streaks). Wherever they are observed, these kinds of streaks are usually aligned with the direction of slip and are generally understood to be linked to aseismic slip (Rubin et al., 1999), which in our case agrees with afterslip models (Figure 8a). It remains to be seen whether these streaks are permanent features, in which case their presence might imply regular aseismic slip in the region, although slow slip events have never been detected here.

It remains unclear however what these lineations could be caused by. Waldhauser et al. (2004) suggested that they might mark a sharp slip gradient at the edge of slip patches (Sammis & Rice, 2001), though that would not fully explain why they are oriented in the dip direction. They may otherwise be structural in origin. In Japan, lineations have been observed at 60–70 km depth, where authors found that they were associated with near-source anisotropy, with higher Vp/Vs in the direction of the streaks, thus underlining the likely role of structural heterogeneity (Huang et al., 2025). One possibility is that they are associated with corrugations in the plate interface, potentially matching km-long physical corrugations observed in other shallow megathrust regions (e.g., Edwards et al., 2018), although it seems unlikely that such structures would have been preserved this deep into the subduction. Perhaps these lineations are fluid conduits, as suggested by Ghosh et al. (2010), though in our case we find no migration to suggest the seismicity is directly related to fluid flow. Lineations could also arise from blocks of resistant rock smeared along the fault zone, like underplated intact oceanic crustal fragments (Behr et al., 2021), or perhaps mantle wedge material entrained through basal erosion, which would be compatible with the idea by K. Wang et al. (2020) that the presence of the LB is linked to the lizardite-antigorite transition. In similar fashion, Ide (2010) proposed that the tremor streaks observed in Nankai could reflect the tracks of seamounts undergoing subduction, perhaps eroding the upper plate and leading to the incorporation of upper plate rocks into the subduction channel. A similar process could explain our observations, although the length scale differs significantly. Alternatively, if we consider that at this depth the interface consists of a block-in-matrix layer (Behr et al., 2021), then these lineations may result from a jamming of this mélange belt (Fagereng & Sibson, 2010). Interactions between clasts can lead to the formation of force chains at a low angle to the plate interface dip, which can lead to brittle failure within clasts, sometimes simultaneously or in close succession (Beall et al., 2019). Thus we could explain the patchiness of the seismicity by the occasional presence of aligned clasts jamming an otherwise mostly viscously deforming mélange belt. Although this is difficult to test, the presence in these lineations of neighboring repeating earthquake families with different focal mechanisms could be a good way to add credence to this hypothesis, although it is outside the scope of our current work.

5. Conclusion

Using modern AI picking and association algorithms, we created a new and enhanced seismic catalog for the Maule aftershock sequence with double-difference locations in a 3D model. We find that the statistical properties and main features of this catalog remain similar to what previous catalogs have shown, but are able to resolve fine-scale structures in detail due to increased earthquake density and relative locations. With this new data set, we confirm the existence of a bimodal distribution of the interplate seismicity at depth. When investigating the LB in more detail, we find that the seismicity is organized into non-overlapping planes of seismicity existing within a ~1.6 km thick layer. Furthermore, much of the seismicity there tends to form 100 m to km scale lineations aligned in dip direction. We interpret these to be the result of either individual blocks smeared along the subduction zone, or of aligned blocks jamming the subduction.

Conflict of Interest

The authors declare no conflicts of interest relevant to this study.

Availability Statement

The IMAD data set is available through EarthScope (https://www.fdsn.org/networks/). The catalog, picks, station list, correlation times, and errors files are available at Chalumeau and Rietbrock (2026).

Acknowledgments

We thank EarthScope, CNRS-INSU, GIPP (GFZ) and GEF/SEIS-UK for providing the onshore seismic instruments and sharing their data, and we thank EarthScope, GFZ and EPOS-France for hosting the data. We thank all those who participated in the station deployment, who serviced the stations or who retrieved the data, and in particular we thank the Servicio Sismológico Nacional de Chile (SSN) and the University of Santiago de Chile for logistical support during the deployment.

References

Aguilar-Suarez, A. L., & Beroza, G. (2025). Picking regional seismic phase arrival times with deep learning. *Seismica*, *4*(1). https://doi.org/10.26443/seismica.v4i1.1431

Agurto, H., Rietbrock, A., Ryder, I., & Miller, M. (2012). Seismic-afterslip characterization of the 2010 Mw 8.8 Maule, Chile, earthquake based on moment tensor inversio. *Geophysical Research Letters*, *39*(20). https://doi.org/10.1029/2012GL053434

Agurto-Detzel, H., Rietbrock, A., Bataille, K., Miller, M., Iwamori, H., & Priestley, K. (2014). Seismicity distribution in the vicinity of the Chile triple junction, Aysén region, southern Chile. *Journal of South American Earth Sciences*, *51*, 1–11. https://doi.org/10.1016/j.jsames.2013.12.011

Bakun, W. H., & Joyner, W. B. (1984). The ML scale in central California. *Bulletin of the Seismological Society of America*, *74*(5), 1827–1843. https://doi.org/10.1785/BSSA0740051827

Beall, A., Fagereng, Å., & Ellis, S. (2019). Fracture and weakening of jammed subduction shear zones, leading to the generation of slow slip events. *Geochemistry, Geophysics, Geosystems*, *20*(11), 4869–4884. https://doi.org/10.1029/2019GC008481

Bedford, J., Moreno, M., Baez, J. C., Lange, D., Tilmann, F., Rosenau, M., et al. (2013). A high-resolution, time-variable afterslip model for the 2010 Maule Mw = 8.8, Chile megathrust earthquake. *Earth and Planetary Science Letters*, *383*, 26–36. https://doi.org/10.1016/j.epsl.2013.09.020

Behr, W. M., Gerya, T. V., Cannizzaro, C., & Blass, R. (2021). Transient slow slip characteristics of frictional-viscous subduction megathrust shear zones. *AGU Advances*, *2*(3), e2021AV000416. https://doi.org/10.1029/2021AV000416

Bohm, M., Lüth, S., Echtler, H., Asch, G., Bataille, K., Bruhn, C., et al. (2002). The southern andes between 36° and 40°S latitude: Seismicity and average seismic velocities. *Tectonophysics*, *356*(4), 275–289. https://doi.org/10.1016/S0040-1951(02)00399-2

Bonali, F. L., Tibaldi, A., Corazzato, C., Tormey, D., & Lara, L. (2013). Quantifying the effect of large earthquakes in promoting eruptions due to stress changes on magma pathway: The Chile case. *Tectonophysics*, *583*, 54–67. https://doi.org/10.1016/j.tecto.2012.10.025

Boneh, Y., Schottenfels, E., Kwong, K., van Zelst, I., Tong, X., Eimer, M., et al. (2019). Intermediate-depth earthquakes controlled by incoming plate hydration along bending-related faults. *Geophysical Research Letters*, *46*(7), 3688–3697. https://doi.org/10.1029/2018GL081585

Calle-Gardella, D., Comte, D., Farías, M., Roecker, S., & Rietbrock, A. (2021). Three-dimensional local earthquake tomography of pre-cenozoic structures in the coastal margin of central Chile: Pichilemu fault system. *Journal of Seismology*, *25*(2), 521–533. https://doi.org/10.1007/s10950-021-09989-w

Campos, J., Hatzfeld, D., Madariaga, R., Lopez, G., Kausel, E., Zollo, A., et al. (2002). A seismological study of the 1835 seismic gap in south-central Chile. *Physics of the Earth and Planetary Interiors*, *132*(1), 177–195. https://doi.org/10.1016/S0031-9201(02)00051-1

Chalumeau, C., Agurto-Detzel, H., Rietbrock, A., Frietsch, M., Oncken, O., Segovia, M., & Galve, A. (2024). Seismological evidence for a multifault network at the subduction interface. *Nature*, *628*(8008), 558–562. https://doi.org/10.1038/s41586-024-07245-y

Chalumeau, C., & Rietbrock, A. (2026). Dataset: New Maule aftershock catalog reveals structure of the deep subduction interface (1.0) [Dataset]. *Zenodo*. https://doi.org/10.5281/zenodo.16942326

Contreras-Reyes, E., Grevemeyer, I., Flueh, E. R., & Reichert, C. (2008). Upper lithospheric structure of the subduction zone offshore of southern Arauco peninsula, Chile, at ~38°S. *Journal of Geophysical Research*, *113*(B7). https://doi.org/10.1029/2007JB005569

Cordell, D., Unsworth, M. J., Diaz, D., Reyes-Wagner, V., Currie, C. A., & Hicks, S. P. (2019). Fluid and melt pathways in the central Chilean subduction zone near the 2010 Maule earthquake (35–36°S) as inferred from magnetotelluric data. *Geochemistry, Geophysics, Geosystems*, *20*(4), 1818–1835. https://doi.org/10.1029/2018GC008167

Cubas, N., Agard, P., & Tissandier, R. (2022). Earthquake ruptures and topography of the Chilean margin controlled by plate interface deformation. *Solid Earth*, *13*(3), 779–792. https://doi.org/10.5194/se-13-779-2022

Dannowski, A., Grevemeyer, I., Kraft, H., Arroyo, I., & Thorwart, M. (2013). Crustal thickness and mantle wedge structure from receiver functions in the Chilean Maule region at 35°S. *Tectonophysics*, *592*, 159–164. https://doi.org/10.1016/j.tecto.2013.02.015

Eberhart-Phillips, D. (1986). Three-dimensional velocity structure in northern California Coast ranges from inversion of local earthquake arrival times. *Bulletin of the Seismological Society of America*, *76*(4), 1025–1052. https://doi.org/10.1785/BSSA0760041025

Edwards, J. H., Kluesner, J. W., Silver, E. A., Brodsky, E. E., Brothers, D. S., Bangs, N. L., et al. (2018). Corrugated megathrust revealed offshore from Costa Rica. *Nature Geoscience*, *11*(3), 197–202. https://doi.org/10.1038/s41561-018-0061-4

Fagereng, Å., & Sibson, R. H. (2010). Mélange rheology and seismic style. *Geology*, *38*(8), 751–754. https://doi.org/10.1130/G30868.1

Farías, M., Comte, D., Roecker, S., Carrizo, D., & Pardo, M. (2011). Crustal extensional faulting triggered by the 2010 Chilean earthquake: The Pichilemu seismic sequence. *Tectonics*, *30*(6). https://doi.org/10.1029/2011TC002888

Franco-Marín, L., Lara, L. E., Basualto, D., Palma, J. L., Gil-Cruz, F., Cardona, C., & Farias, C. (2023). A long time of rest at Llaima volcano following the 2010 MW 8.8 Maule earthquake, Chile. *Journal of Volcanology and Geothermal Research*, *440*, 107858. https://doi.org/10.1016/j.jvolgeores.2023.107858

Ghosh, A., Vidale, J. E., Sweet, J. R., Creager, K. C., Wech, A. G., Houston, H., & Brodsky, E. E. (2010). Rapid, continuous streaking of tremor in Cascadia. *Geochemistry, Geophysics, Geosystems*, *11*(12). https://doi.org/10.1029/2010GC003305

Hayes, G. P., Bergman, E., Johnson, K. L., Benz, H. M., Brown, L., & Meltzer, A. S. (2013). Seismotectonic framework of the 2010 February 27 Mw 8.8 Maule, Chile earthquake sequence. *Geophysical Journal International*, *195*(2), 1034–1051. https://doi.org/10.1093/gji/ggt238

Hicks, S. P., Rietbrock, A., Haberland, C. A., Ryder, I. M. A., Simons, M., & Tassara, A. (2012). The 2010 Mw 8.8 Maule, Chile earthquake: Nucleation and rupture propagation controlled by a subducted topographic high. *Geophysical Research Letters*, *39*(19). https://doi.org/10.1029/2012GL053184

Hicks, S. P., Rietbrock, A., Ryder, I. M., Lee, C. S., & Miller, M. (2014). Anatomy of a megathrust: The 2010 M8.8 Maule, Chile earthquake rupture zone imaged using seismic tomography. *Earth and Planetary Science Letters*, *405*, 142–155. https://doi.org/10.1016/j.epsl.2014.08.028

Huang, Y., Ide, S., Kato, A., Yoshida, K., Jiang, C., & Zhai, P. (2025). Fault material heterogeneity controls deep interplate earthquakes. *Science Advances*, *11*(9), eadr9353. https://doi.org/10.1126/sciadv.adr9353

Ide, S. (2010). Striations, duration, migration and tidal response in deep tremor. *Nature*, *466*(7304), 356–359. https://doi.org/10.1038/nature09251

Kimura, H., Takeda, T., Obara, K., & Kasahara, K. (2010). Seismic evidence for active underplating below the megathrust earthquake zone in Japan. *Science*, *329*(5988), 210–212. https://doi.org/10.1126/science.1187115

Kirby, S., Engdahl, R. E., & Denlinger, R. (1996). Intermediate-depth intraslab earthquakes and arc volcanism as physical expressions of crustal and uppermost mantle metamorphism in subducting slabs. In *Subduction* (pp. 195–214). American Geophysical Union (AGU). https://doi.org/10.1029/GM096p0195

Kiser, E., & Ishii, M. (2011). The 2010 Mw 8.8 Chile earthquake: Triggering on multiple segments and frequency-dependent rupture behavior. *Geophysical Research Letters*, *38*(7). https://doi.org/10.1029/2011GL047140

Klein, E., Fleitout, L., Vigny, C., & Garaud, J. (2016). Afterslip and viscoelastic relaxation model inferred from the large-scale post-seismic deformation following the 2010 Mw 8.8 Maule earthquake (Chile). *Geophysical Journal International*, *205*(3), 1455–1472. https://doi.org/10.1093/gji/ggw086

Lange, D., Rietbrock, A., Haberland, C., Bataille, K., Dahm, T., Tilmann, F., & Flüh, E. R. (2007). Seismicity and geometry of the south Chilean subduction zone (41.5°S–43.5°S): Implications for controlling parameters. *Geophysical Research Letters*, *34*(6). https://doi.org/10.1029/2006GL029190

Lange, D., Tilmann, F., Barrientos, S. E., Contreras-Reyes, E., Methe, P., Moreno, M., et al. (2012). Aftershock seismicity of the 27 February 2010 Mw 8.8 Maule earthquake rupture zone. *Earth and Planetary Science Letters*, *317–318*, 413–425. https://doi.org/10.1016/j.epsl.2011.11.034

Lieser, K., Grevemeyer, I., Lange, D., Flueh, E., Tilmann, F., & Contreras-Reyes, E. (2014). Splay fault activity revealed by aftershocks of the 2010 Mw 8.8 Maule earthquake, central Chile. *Geology*, *42*(9), 823–826. https://doi.org/10.1130/G35848.1

Lin, Y. N., Sladen, A., Ortega-Culaciati, F., Simons, M., Avouac, J., Fielding, E. J., et al. (2013). Coseismic and postseismic slip associated with the 2010 Maule Earthquake, Chile: Characterizing the Arauco Peninsula barrier effect. *Journal of Geophysical Research: Solid Earth*, *118*(6), 3142–3159. https://doi.org/10.1002/jgrb.50207

Lomax, A., Virieux, J., Volant, P., & Berge-Thierry, C. (2000). Probabilistic earthquake location in 3D and layered models, In C. H. Thurber, & N. Rabinowitz (Eds.) *Advances in seismic event location*. Springer Netherlands (Modern Approaches in Geophysics). (pp. 101–134). https://doi.org/10.1007/978-94-015-9536-0_5

Lomax, A., Michelini, A., & Curtis, A. (2014). Arthquake location, direct, global-search methods, In R. A. Meyers (Ed.) *Encyclopedia of complexity and systems science*. Springer. (pp. 1–33). https://doi.org/10.1007/978-3-642-27737-5_150-2

Lorito, S., Romano, F., Atzori, S., Tong, X., Avallone, A., McCloskey, J., et al. (2011). Limited overlap between the seismic gap and coseismic slip of the great 2010 Chile earthquake. *Nature Geoscience*, *4*(3), 173–177. https://doi.org/10.1038/ngeo1073

Maksymowicz, A., Chadwell, C. D., Ruiz, J., Tréhu, A. M., Contreras-Reyes, E., Weinrebe, W., et al. (2017). Coseismic seafloor deformation in the trench region during the Mw8.8 Maule megathrust earthquake. *Scientific Reports*, *7*(1), 45918. https://doi.org/10.1038/srep45918

Menant, A., Angiboust, S., Gerya, T., Lacassin, R., Simoes, M., & Grandin, R. (2020). Transient stripping of subducting slabs controls periodic forearc uplift. *Nature Communications*, *11*(1), 1823. https://doi.org/10.1038/s41467-020-15580-7

Michelini, A., Cianetti, S., Gaviano, S., Giunchi, C., Jozinović, D., & Lauciani, V. (2021). INSTANCE – The Italian seismic dataset for machine learning. *Earth System Science Data*, *13*(12), 5509–5544. https://doi.org/10.5194/essd-13-5509-2021

Moreno, M., Haberland, C., Oncken, O., Rietbrock, A., Angiboust, S., & Heidbach, O. (2014). Locking of the Chile subduction zone controlled by fluid pressure before the 2010 earthquake. *Nature Geoscience*, *7*(4), 292–296. https://doi.org/10.1038/ngeo2102

Moreno, M., Melnick, D., Rosenau, M., Baez, J., Klotz, J., Oncken, O., et al. (2012). Toward understanding tectonic control on the Mw 8.8 2010 Maule Chile earthquake. *Earth and Planetary Science Letters*, *321–322*, 152–165. https://doi.org/10.1016/j.epsl.2012.01.006

Moscoso, E., Grevemeyer, I., Contreras-Reyes, E., Flueh, E. R., Dzierma, Y., Rabbel, W., & Thorwart, M. (2011). Revealing the deep structure and rupture plane of the 2010 Maule, Chile earthquake (Mw=8.8) using wide angle seismic data. *Earth and Planetary Science Letters*, *307*(1), 147–155. https://doi.org/10.1016/j.epsl.2011.04.025

Münchmeyer, J., Woollam, J., Rietbrock, A., Tilmann, F., Lange, D., Bornstein, T., et al. (2022). Which picker fits my data? A quantitative evaluation of deep learning based seismic pickers. *Journal of Geophysical Research: Solid Earth*, *127*(1), e2021JB023499. https://doi.org/10.1029/2021JB023499

Nacif, S., Triep, E. G., Spagnotto, S. L., Aragon, E., Furlani, R., & Álvarez, O. (2015). The flat to normal subduction transition study to obtain the Nazca plate morphology using high resolution seismicity data from the Nazca plate in Central Chile. *Tectonophysics*, *657*, 102–112. https://doi.org/10.1016/j.tecto.2015.06.027

Palo, M., Tilmann, F., Krüger, F., Ehlert, L., & Lange, D. (2014). High-frequency seismic radiation from Maule earthquake (Mw 8.8, 2010 February 27) inferred from high-resolution backprojection analysis. *Geophysical Journal International*, *199*(2), 1058–1077. https://doi.org/10.1093/gji/ggu311

Pritchard, M. E., Jay, J. A., Aron, F., Henderson, S. T., & Lara, L. E. (2013). Subsidence at southern Andes volcanoes induced by the 2010 Maule, Chile earthquake. *Nature Geoscience*, *6*(8), 632–636. https://doi.org/10.1038/ngeo1855

Rietbrock, A., Ryder, I., Hayes, G., Haberland, C., Comte, D., Roecker, S., & Lyon-Caen, H. (2012). Aftershock seismicity of the 2010 Maule Mw=8.8, Chile, earthquake: Correlation between co-seismic slip models and aftershock distribution? *Geophysical Research Letters*, *39*(8), https://doi.org/10.1029/2012GL051308

10.1029/2025JB032839

Roecker, S., & Russo, R. (2010). RAMP response for 2010 Chile earthquake. *International Federation of Digital Seismograph Networks*. https://doi.org/10.7914/SN/XY_2010

Rubin, A. M., Gillard, D., & Got, J.-L. (1999). Streaks of microearthquakes along creeping faults. *Nature*, *400*(6745), 635–641. https://doi.org/10.1038/23196

Ruiz, J. A., & Contreras-Reyes, E. (2015). Outer rise seismicity boosted by the Maule 2010 Mw 8.8 megathrust earthquake. *Tectonophysics*, *653*, 127–139. https://doi.org/10.1016/j.tecto.2015.04.007

Ryder, I., Rietbrock, A., Kelson, K., Bürgmann, R., Floyd, M., Socquet, A., et al. (2012). Large extensional aftershocks in the continental forearc triggered by the 2010 Maule earthquake, Chile. *Geophysical Journal International*, *188*(3), 879–890. https://doi.org/10.1111/j.1365-246X.2011.05321.x

Sammis, C. G., & Rice, J. R. (2001). Repeating earthquakes as low-stress-drop events at a border between locked and creeping fault patches. *Bulletin of the Seismological Society of America*, *91*(3), 532–537. https://doi.org/10.1785/0120000075

Schaff, D. P., & Richards, P. G. (2014). Improvements in magnitude precision, using the statistics of relative amplitudes measured by cross correlation. *Geophysical Journal International*, *197*(1), 335–350. https://doi.org/10.1093/gji/ggt433

Sladen, A., & Trevisan, J. (2018). Shallow megathrust earthquake ruptures betrayed by their outer-trench aftershocks signature. *Earth and Planetary Science Letters*, *483*, 105–113. https://doi.org/10.1016/j.epsl.2017.12.006

Spagnotto, S., Triep, E., Giambiagi, L., & Lupari, M. (2015). Triggered seismicity in the Andean arc region via static stress variation by the MW = 8.8, February 27, 2010, Maule earthquake. *Journal of South American Earth Sciences*, *63*, 36–47. https://doi.org/10.1016/j.jsames.2015.06.009

Thurber, C., & Eberhart-Phillips, D. (1999). Local earthquake tomography with flexible gridding. *Computers & Geosciences*, *25*(7), 809–818. https://doi.org/10.1016/S0098-3004(99)00007-2

Thurber, C., Zhang, H., Brocher, T., & Langenheim, V. (2009). Regional three-dimensional seismic velocity model of the crust and uppermost mantle of northern California. *Journal of Geophysical Research*, *114*(B1). https://doi.org/10.1029/2008JB005766

Trugman, D. T., Chamberlain, C. J., Savvaidis, A., & Lomax, A. (2023). GrowClust3D.jl: A julia package for the relative relocation of earthquake hypocenters using 3D velocity models. *Seismological Research Letters*, *94*(1), 443–456. https://doi.org/10.1785/0220220193

Trugman, D. T., & Shearer, P. M. (2017). GrowClust: A hierarchical clustering algorithm for relative earthquake relocation, with application to the Spanish springs and sheldon, Nevada, earthquake sequences. *Seismological Research Letters*, *88*(2A), 379–391. https://doi.org/10.1785/0220160188

Umino, N., Hasegawa, A., & Matsuzawa, T. (1995). sP depth phase at small epicentral distances and estimated subducting plate boundary. *Geophysical Journal International*, *120*(2), 356–366. https://doi.org/10.1111/j.1365-246X.1995.tb01824.x

van Keken, P. E., Hacker, B. R., Syracuse, E. M., & Abers, G. A. (2011). Subduction factory: 4. Depth-dependent flux of H2O from subducting slabs worldwide. *Journal of Geophysical Research*, *116*(B1), B01401. https://doi.org/10.1029/2010JB007922

Vigny, C., Socquet, A., Peyrat, S., Ruegg, J. C., Métois, M., Madariaga, R., et al. (2011). The 2010 Mw 8.8 Maule megathrust Earthquake of Central Chile, monitored by GPS. *Science*, *332*(6036), 1417–1421. https://doi.org/10.1126/science.1204132

Vilotte, J.-P., & RESIF (2011). Seismic network XS:CHILE MAULE aftershock temporary experiment (RESIF-SISMOB). *RESIF - Réseau Sismologique et géodésique Français*. https://doi.org/10.15778/RESIF.XS2010

Waldhauser, F., & Ellsworth, W. L. (2000). A double-difference earthquake location algorithm: Method and application to the northern Hayward fault, California. *Bulletin of the Seismological Society of America*, *90*(6), 1353–1368. https://doi.org/10.1785/0120000006

Waldhauser, F., Ellsworth, W. L., Schaff, D. P., & Cole, A. (2004). Streaks, multiplets, and holes: High-resolution spatio-temporal behavior of Parkfield seismicity. *Geophysical Research Letters*, *31*(18), https://doi.org/10.1029/2004GL020649

Wang, D., & Mori, J. (2011). Frequency-dependent energy radiation and fault coupling for the 2010 Mw8.8 Maule, Chile, and 2011 Mw9.0 Tohoku, Japan, earthquakes. *Geophysical Research Letters*, *38*(22). https://doi.org/10.1029/2011GL049652

Wang, K., Huang, T., Tilmann, F., Peacock, S. M., & Lange, D. (2020). Role of serpentinized mantle wedge in affecting megathrust seismogenic behavior in the area of the 2010 M = 8.8 Maule Earthquake. *Geophysical Research Letters*, *47*(22), e2020GL090482. https://doi.org/10.1029/2020GL090482

Wimpenny, S., Craig, T., & Marcou, S. (2023). Re-Examining temporal variations in intermediate-depth seismicity. *Journal of Geophysical Research: Solid Earth*, *128*(6), e2022JB026269. https://doi.org/10.1029/2022JB026269

Woollam, J., Münchmeyer, J., Tilmann, F., Rietbrock, A., Lange, D., Bornstein, T., et al. (2022). SeisBench—A toolbox for machine learning in seismology. *Seismological Research Letters*, *93*(3), 1695–1709. https://doi.org/10.1785/0220210324

Woollam, J., Rietbrock, A., Leitloff, J., & Hinz, S. (2020). HEX: Hyperbolic event eXtractor, a seismic phase associator for highly active seismic regions. *Seismological Research Letters*, *91*(5), 2769–2778. https://doi.org/10.1785/0220200037

Yue, H., Lay, T., Rivera, L., An, C., Vigny, C., Tong, X., & Báez Soto, J. C. (2014). Localized fault slip to the trench in the 2010 Maule, Chile Mw = 8.8 earthquake from joint inversion of high-rate GPS, teleseismic body waves, InSAR, campaign GPS, and tsunami observations. *Journal of Geophysical Research: Solid Earth*, *119*(10), 7786–7804. https://doi.org/10.1002/2014JB011340

Zhu, W., & Beroza, G. C. (2019). PhaseNet: A deep-neural-network-based seismic arrival-time picking method. *Geophysical Journal International*, *216*(1), 261–273. https://doi.org/10.1093/gji/ggy423

References From the Supporting Information

Hayes, G. P., Moore, G. L., Portner, D. E., Hearne, M., Flamme, H., Furtney, M., & Smoczyk, G. M. (2018). Slab2, a comprehensive subduction zone geometry model. *Science*, *362*(6410), 58–61. https://doi.org/10.1126/science.aat4723

Schorlemmer, D., & Woessner, J. (2008). Probability of detecting an earthquake. *Bulletin of the Seismological Society of America*, *98*(5), 2103–2117. https://doi.org/10.1785/0120070105

Woessner, J., & Wiemer, S. (2005). Assessing the quality of earthquake catalogues: Estimating the magnitude of completeness and its uncertainty. *Bulletin of the Seismological Society of America*, *95*(2), 684–698. https://doi.org/10.1785/0120040007